Mesoporous carbon with extremely low micropore content synthesized from graphene oxide modified with alkali metal nitrates

Zhao Li, Moeto Toyota, Takahiro Ohkubo*

Department of Chemistry, Graduate School of Natural Science and Technology, Okayama University, 3-1-1 Tsushimanaka, Kita-ku, Okayama 700-8530, Japan

ABSTRACT: High-temperature thermal exfoliation is a simple, rapid, and cost-efficient method for transforming graphene oxide (GO) materials into reduced graphene oxide (rGO) materials. In this study, GO materials were dispersed with alkali metal nitrates (MNO$_3$), leading to the preparation of porous rGO materials characterized by high specific surface areas (SSAs) and pore volume via high-temperature thermal exfoliation. Experimental data indicate that the metal cations of MNO$_3$ tend to react directly with the oxygen functional groups (OFG) of GO, modulating the OFG content. Simultaneously, nitrate anions have preferential interaction with alkali metal ions and adhere to the surface of the GO. The presence of MNO$_3$ on the surface of GO facilitates the thermal exfoliation process and leads to the formation of structures with an extremely high proportion of mesoporous content. The isothermal gas adsorption results show that the exfoliation efficiency of the samples activated with different nitrate salts decreases in the order rGO-KNO$_3$ > rGO-NaNO$_3$ > rGO-LiNO$_3$. Among these samples, rGO modified with KNO$_3$ exhibited the greatest exfoliation efficiency, with a mesopore-to-micropore volume ratio of 22.4, more than 1.7 times that of rGO. Its SSA and pore volume were 359 m^2 g^{-1} and 1.26 cm^3 g^{-1}, respectively. These values significantly surpass those of rGO. Our research findings demonstrate that activation with MNO$_3$ significantly increases the SSA and pore volume of the GO material after high-temperature annealing.

Keywords: Mesoporous carbon, Alkali metal nitrates, Oxygen functional groups, Activation, Thermal exfoliation

* Corresponding author: Takahiro Ohkubo, Email: ohkubo@okayama-u.ac.jp

Introduction

Recently, graphene materials have garnered significant attention owing to their large surface areas, excellent electrical conductivity, and exceptional mechanical properties [1, 2]. Graphene oxide (GO), a derivative of graphene, has emerged as a noteworthy material due to its abundance of oxygen functional groups (OFG) and significant scope for application. The resulting reduced form, known as reduced graphene oxide (rGO), has been applied in diverse fields, such as adsorbents, photocatalysts, supercapacitors, and electronic devices [3, 4]. It is widely acknowledged that various methods exist for the reduction of GO, including thermal reduction, chemical reduction, microwave reduction, and solvent/hydrothermal reduction [5, 6]. Among these technologies, thermal reduction has gained considerable prominence owing to its advantages, which include high yield, the utilization of non-chemical reagents, and minimal time consumption [7–11]. During the process of high-temperature thermal reduction, several key factors should be considered, including the OFG content, heating rate, and the pressure difference between the internal and external environments of the GO nanosheets [12, 13]. These factors directly affect the exfoliation dynamics of GO during high-temperature thermal exfoliation. Consequently, they govern the resultant surface morphology and specific surface area (SSA) of the product, and hence careful consideration of these factors can yield significant improvements in the application potential of the material.

Recently, many researchers have studied the high-temperature thermal reduction of GO. For instance, Somphonsane and co-workers observed that structural changes in GO occur within the temperature range of 200–300 °C during thermal exfoliation. With increasing heating temperatures, carbon atoms within GO are transformed into CO_2 and CO, resulting in additional defects, Additionally, they studied the morphology and electrical properties of thermally reduced free-standing GO papers [14]. The work of Kim and co-workers involved doping GO materials with alkali metals, resulting in rGO materials with enhanced conductivity upon subsequent thermal reduction. After doping the sample with alkali metals followed by thermal reduction, the sheet resistance of the doped samples decreased significantly, from 311.0 kΩ sq^{-1} to as low as 32.1 kΩ sq^{-1} [15]. Nyamori and co-workers synthesized GO by reacting graphite with sodium nitrate and adjusting the oxygen content of the sample by varying the mass ratio of graphite to sodium nitrate and the reaction time. Their study examined the effect of oxygen content on the physical and chemical properties of GO, ultimately affecting its specific surface area and porosity after thermal

exfoliation [16]. The studies discussed above primarily focus on the kinetics of thermal exfoliation and the application of prepared materials in electrochemistry. Although thermal exfoliation of pure GO can produce relatively high SSA, it usually only produces structures with a considerable proportion of micropores and mesopores [17].

To the best of our knowledge, there is no such publication exploring the role of alkali metal nitrate in promoting the activation of GO nanosheets during high-temperature calcination. Upon introducing alkali metal nitrate (MNO$_3$) into the GO structure, the M^+ ions tend to accumulate near the GO nanosheets, owing to various interactions [18, 19]. Nitrate anions also have preferential interaction with alkali metal ions and adhere to the surface of the GO. Hence, further research is needed to unveil the mechanism behind the effect of MNO$_3$ in activating the high-temperature thermal exfoliation of GO.

In this study, a series of MNO$_3$ compounds (LiNO$_3$, NaNO$_3$, or KNO$_3$) were used as activating agents for GO at the same molar concentration. After thorough mixing, this procedure yielded three distinct GO samples, denoted GO-MNO$_3$ (where M represents the alkali metal Li, Na, or K). Subsequent high-temperature calcination produced three corresponding samples, which contained extremely high proportions of mesoporous content. In the subsequent sections of the manuscript, we present and rigorously discuss the specific experimental procedures and results obtained.

Experimental

2.1. Chemicals and materials

Graphite powder (99.9995 %) was obtained from Alfa Aesar, USA. Potassium permanganate (KMnO$_4$, 99.3 %), concentrated sulfuric acid (H$_2$SO$_4$, 97 %), hydrogen peroxide (H$_2$O$_2$, 30 %), LiNO$_3$ (99.9 %), NaNO$_3$ (99.9 %), KNO$_3$ (99.9 %), RbNO$_3$ (99.9 %), CsNO$_3$ (99.9 %), and copper(II) sulfate pentahydrate (CuSO$_4$·5H$_2$O, 99.5 %) were purchased from Fujifilm Wako Pure Chemical Co, Japan. Hydrochloric acid (HCl, 35 %) was supplied by Nacalai Tesque, Inc., Japan.

2.2. Synthesis of GO samples

The GO materials were synthesized using a modified Hummer's method [20, 21]. Typically, 1.0 g of 200-mesh graphite powder was mechanically stirred in an ice bath, and 25 mL of 97 % H$_2$SO$_4$ was added to a 300 mL beaker. Subsequently, 3.0 g of KMnO$_4$ was slowly added while maintaining

the suspension temperature below 10 ℃. The reaction system was then transferred to a 35 ℃ water bath and vigorously stirred for approximately 2 h. Following this, 100 mL of water was added dropwise, and then the solution was heated to 90 ℃ with stirring for an additional 15 min. Next, 5 mL of H_2O_2 (30%) was added dropwise. The mixture was filtered, and the resulting precipitate was washed six times with a 5% aqueous HCl solution to remove metal ions and then rinsed with deionized water to adjust the pH to 7. The obtained samples were dispersed in 300 mL of water to form an aqueous GO dispersion. Finally, the GO dispersion was dialyzed for 2 weeks to remove residual acid and metal substances. After careful stirring of the resulting aqueous GO dispersion, the dispersion was suction-filtered to form a filter cake, which was air-dried and ground into powder for later use.

2.3. Synthesis of GO-*M*NO_3 samples

The prepared GO (0.1 g) was added to 100 mL of water, yielding a 1 mg mL^{-1} GO dispersion. For the composite process, 0.05 mol of *M*NO_3 was added to the GO dispersion. After that, the mixture was sonicated for 60 min to ensure uniform dispersion of the materials. Subsequently, the mixed solution was stirred for 24 h at a speed of 500 rpm. The resulting solution was then filtered, resulting in the formation of a membrane, which was subsequently dried and ground into a powder. The obtained samples of the successfully modified GO were labeled GO-*M*NO_3 (*M* = K, Na, or Li).

2.4. Thermal exfoliation of GO-*M*NO_3

GO and GO-*M*NO_3 samples of the same weight were heated in the central zone of a tube furnace. To eliminate oxygen from the tube, high-purity Ar gas flowed at a rate of 100 mL min^{-1} for 60 min. For the heating process, for the exfoliation of the GO and GO-*M*NO_3 samples, the temperature was ramped at a rate of 10 ℃ min^{-1} from room temperature to 800 ℃. Once the temperature reached 800 ℃, it was maintained for 60 min. Subsequently, the samples were allowed to cool down naturally to room temperature. The resultant thermally treated samples were labeled rGO and rGO-*M*NO_3.

2.5. Characterization

Nitrogen adsorption–desorption isotherms were measured at 77 K using a BELSORP-max instrument (Microtrac BEL). The pore structures were analyzed using the α_s-plot analysis method, which revealed the SSAs and pore volumes [22, 23]. X-ray diffraction (XRD) patterns were acquired using a MiniFlexII diffractometer (Rigaku Ltd.) with Cu Kα radiation (0.154 nm) at diffraction angles between 5 and 30°. Fourier-transform infrared (FTIR) spectra were obtained using the KBr method and an FTIR spectrophotometer (FTS4000MXK, Digilab, Randolph) at room temperature. The spectra were recorded over a wavenumber range spanning 500 to 2000 cm^{-1}. Thermogravimetry (TG) and Differential Thermal Analysis (DTA) measurements were obtained using a Thermal plus EVO2 instrument (Rigaku Ltd.) under an Ar atmosphere. The temperature range covered was 20–800 ℃ and the heating rate was 2 ℃ min^{-1}. X-ray photoelectron spectroscopy (XPS) measurements were acquired using a JEOL JPS-9030 instrument. The UV-Vis spectrometer (JASCO V-770) was used to test the concentration of heavy metal ions in aqueous solutions.

3. Results and discussion

3.1. Pore structure characterization

The N_2 adsorption–desorption isotherms and pore-size distribution of the samples are depicted in Fig. 1 and Fig. S1, in the Supplementary material, respectively. According to IUPAC guidelines, the isotherms of rGO-$LiNO_3$, rGO-$NaNO_3$, rGO-KNO_3, and rGO can be classified as type IV isotherms [24]. Type IV isotherms are typically observed for mesoporous materials and exhibit hysteresis due to the liquid-like adsorbed phase of N_2 within the pores. The hysteresis loops observed in these samples are categorized as H4-type loops, indicating the presence of interconnected slit pores [25]. Fig. S1 depicts the pore size distribution curves of distinct samples, obtained by the non-local density functional theory (NLDFT) method. As shown in Fig. S1, rGO and rGO-$M$$NO_3$ materials have mostly mesoporous structures, while containing a small amount of micropores and macropores. The outcomes also prove that the synthesized samples are typical mesoporous materials. A comparison of the NLDFT data of different samples in Fig. S1 reveals that the prepared rGO-$M$$NO_3$ exhibit a higher proportion of mesoporous structure than that of pure rGO. The measurement results were analyzed using the α_s-plot method and the pore parameters are listed in Table 1, where the micropore and mesopore parameters are shown separately. Here, we assumed that the SSA of macropore is negligible because all adsorbents consist of both mesopore and a small amount of micropore as shown in Fig. S1. As shown in Table 1, the values for the micropore SSA and volume are similar among the four samples, but there are significant differences between the values for the mesopore SSAs and volumes. rGO exhibits the smallest mesopore volume and SSA. After activation with alkali metal nitrates, there is a significant increase in these values for all the samples, with rGO-KNO_3 displaying the most developed mesoporous structure. The pore surface area and volume in the mesopore region for this sample are 336 $m^2\ g^{-1}$ and 1.21 $cm^3\ g^{-1}$, respectively, significantly surpassing those of rGO and exceeding the values for the rGO-$LiNO_3$ and rGO-$NaNO_3$ samples. In addition, the a_{meso}/a_{micro} and W_{meso}/W_{micro} ratios for rGO-KNO_3 are 14.6 and 22.4, respectively. These values are higher than those of the rGO sample, which has ratios of 10.4 and 13.2, respectively. Meanwhile, for rGO-$LiNO_3$ and rGO-$NaNO_3$, the a_{meso}/a_{micro} ratios are 15.2 and 15.2, while the W_{meso}/W_{micro} ratios are 19.8 and 20.4, respectively. These ratios are also higher than the corresponding values for the rGO sample. The aforementioned results indicate that $M$$NO_3$ can facilitate the high-temperature activation of the thermal exfoliation process of GO, enhancing the

proportion of mesopores in the resulting product. Previously published research results show that the mesopore/micropore volume ratio of typical rGO samples ranges from 0.2 to 6.5 [8, 17]. Although these samples can be defined as mesoporous materials, they still retain abundant microporous structures on their surfaces. Therefore, the significant difference between rGO-MNO$_3$ and typical rGO is that the mesopore content of rGO-MNO$_3$ is much higher than the micropore content. It is noteworthy that the pore surface area and volume of the modified rGO samples increased after the addition of MNO$_3$; for example, the values increased from 206 m^2 g^{-1} and 0.61 cm^3 g^{-1} for rGO to 359 m^2 g^{-1} and 1.26 cm^3 g^{-1} for rGO-KNO$_3$, respectively. The reason why the modified rGO sample has a more developed pore structure is because the process of activating the GO nanosheets triggers a series of redox chemical reactions during high-temperature thermal treatment. The activation process consumes more carbon atoms, produces more gases such as CO$_2$ and CO, and ultimately creates pores on the carbon surface. Therefore, the SSA and pore volume of rGO-MNO$_3$ are greater. It can be seen from Table 1 that the SSAs and pore volumes of the different samples decrease in the order rGO-KNO$_3$ > rGO-NaNO$_3$ > rGO-LiNO$_3$. Based on the mechanism discussed above, we can conclude that rGO modified with MNO$_3$ contains a higher proportion of mesopores than that of rGO, and hence it also has an increased SSA and pore volume. Furthermore, the conclusion mentioned above was proven by employing RbNO$_3$ and CsNO$_3$ to assess the thermal exfoliation effect of activated GO. The test results are presented in Fig. S2, the adsorption performance is superior to that of rGO materials, and the rGO-RbNO$_3$ and rGO-CsNO$_3$ exhibit an exceptionally high content of mesoporous structure. Consequently, the result suggests that nitrate salts can facilitate the thermal exfoliation of GO to generate mesoporous carbon materials with minimal microporosity.

3.2. Microcrystalline and surface structure

Fig. 2a displays the XRD patterns of the GO and GO-MNO$_3$ samples. The (001) diffraction peak of the GO sample appears at 11.45°, corresponding to an interplanar spacing of 0.773 nm, according to Bragg's law [26]. From the data listed in Table 2, it is apparent that the peak positions of the GO-MNO$_3$ were shifted and spanned a wider region of diffraction angles. Importantly, the full width at half maximum (FWHM) of the (001) peaks for the GO-MNO$_3$ samples were wider than those of GO owing to the introduction of the MNO$_3$ salts. The origin of this phenomenon is two-fold: first,

the effect of the MNO$_3$ salts is to reduce the interplanar spacing of the original crystal structure of GO; second, the monovalent metal cations tend to react with the OFG in GO and disrupt its local crystalline structure. The diffraction peak positions of GO-MNO$_3$ fluctuate in the range of 11.55–11.92°, which is consistent with the results reported in the previous literature [18, 27]. Therefore, the above-discussed XRD analysis conclusively demonstrates the successful introduction of MNO$_3$ salts into the GO structure. In Fig. S3, rGO exhibits a diffraction peak at 26.42°, which is assigned to the (002) graphitic plane of rGO. Additionally, (002) peaks at 26.56, 26.55, and 25.91° are seen in the XRD patterns of rGO-LiNO$_3$, rGO-NaNO$_3$, and rGO-KNO$_3$, respectively. From this, we can draw two specific conclusions: first, the rGO and rGO-MNO$_3$ samples have similar microscopic crystal structures; second, after high-temperature thermal reduction, the spacing between carbon nanosheet layers decreases, indicating that the adsorbed water molecules and OFG between GO nanolayers were eliminated. Moreover, the (002) diffraction peak of rGO-MNO$_3$ broadened at the half maximum, indicating a lower degree of graphitization and an increase in the disorder of the lamellar stacking.

The FTIR bands observed at 1720, 1625, 1384, 1240, and 1090 cm^{-1} (Fig. 2b) correspond to the carboxyl/carbonyl C=O, aromatic C=C, carboxyl C–O, epoxy/ether C–O, and alkoxy/alkoxide C–O, respectively. These spectral features are characteristic of GO, confirming the successful synthesis of GO materials. Comparative analysis of the GO-MNO$_3$ samples and GO material reveals notable differences. In the FTIR spectra, the C=O to C=C absorption intensity ratios of GO-LiNO$_3$, GO-NaNO$_3$, and GO-KNO$_3$ are 0.93, 0.94, and 0.95 respectively. These values are less than that of GO (0.99). The reduction in this ratio stems from the tendency of M^+ to coordinate with C=O groups, effectively consuming a considerable number of them. It is apparent that the absorption band intensity associated with C–O–C groups nearly disappears when M^+ ions are introduced into the GO structure. This is a result of M^+ triggering epoxide ring-opening reactions, effectively reducing the C–O–C group content. In addition, M^+ tends to interact with the carboxyl groups of GO, inducing the cleavage of the carboxyl groups into new C-O and C=C bonds. This process increases the amount of aromatic C=C groups [28]. The aforementioned observations collectively indicate that a series of chemical reactions take place after the introduction of M^+ ions into the GO structure. Inevitably, these reactions alter the chemical properties of the GO, consequently influencing the high-temperature thermal exfoliation of the MNO$_3$-GO samples.

The almost complete disappearance of the carboxyl C–O and alkoxy/alkoxide C–O bands in the spectra of the rGO and rGO-MNO$_3$ samples, compared to the spectra of the corresponding GO and GO-MNO$_3$ samples, should be highlighted (Fig. S4). This observation underlines the fact that the high-temperature thermal exfoliation process effectively eliminates a substantial portion of the OFG [29]. The abovementioned findings support the conclusion that MNO$_3$ contributes to the activation of thermal exfoliation for the preparation of GO nanosheets. This activation process facilitates the removal of OFG and promotes the overall thermal exfoliation process, leading to the production of rGO-MNO$_3$ nanosheets.

3.3. Thermal stability analysis

The results of the TG measurements are depicted in Fig. 3 and Table 3. For the pure GO, the weight reduction in the TG curve can be categorized into three stages: the first stage corresponds to the loss of adsorbed interlayer water (T < 100 ℃), the second stage to unstable OFG (eg. epoxy and hydroxyl) decomposition (100 ℃ < T < 300 ℃), and the third stage to stable OFG (eg. carboxyl, ether and carbonyl) decomposition (T > 300 ℃), respectively. However, in the GO-MNO$_3$, the decomposition of nitrate salt is involved (T > 650 ℃) [30, 31]. These results yield a notable observation: the unstable OFG weight loss temperature of GO-MNO$_3$ is shifted toward lower temperatures compared to that of GO. The phenomenon is mainly caused by the interaction between M^+ and the OFG. M^+ species can react with hydroxyl groups and form new chemical bonds, such as C–O–M bonds. Additionally, M^+ also reacts with epoxide groups, leading to the transformation of high-energy C–O–C bonds into lower-energy C–O–M bonds. Breaking the newly formed chemical bonds requires less activation energy as they have lower energy barriers. According to the Arrhenius equation, the lower the activation energy, the lower the reaction temperature. Therefore, the exothermic peaks of all the modified GO samples are shifted to lower temperatures with respect to that of pristine GO [28, 32–33]. As shown in Fig. S5 and Table S1, it is worth noting that there is no significant variation in the weight loss temperature of the unstable OFG among the three GO-MNO$_3$ samples, which are all approximately 165 ℃. The unstable OFG weight loss of GO-MNO$_3$ is lower than that of GO. This reduction points to the role of M^+ in reacting with the OFG, consequently reducing the weight loss attributed to C–O–C groups [34]. In addition, GO-MNO$_3$ exhibits a distinct weight loss process at 650 ℃, which can be attributed to the thermal

decomposition of nitrate salt, resulting in the production of nitrite, CO_2, and other substances [35]. Hence, the weight loss temperatures observed in the thermal decomposition of three different alkali metal nitrates are similar, indicating that the decomposition process primarily involves introduced nitrate salts. The aforementioned results demonstrate that MNO$_3$ can facilitate the GO thermal exfoliation process.

3.4. Surface chemistry of GO-MNO$_3$ and rGO-MNO$_3$

Fig. S6a shows the survey XPS data for the samples acquired before thermal reduction. A survey of the literature reveals that the following elements appear at the specified energies: C 1s at 284 eV, O 1s at 532 eV, N 1s at 400 eV, Li 1s at 55 eV, Na 1s at 1070 eV, and K 2s at 377 eV and K 2p at 293 eV [15, 36–37]. Notably, the survey spectra of the GO-MNO$_3$ samples exhibit distinct M^+ bands, indicating the successful incorporation of various M^+ ions into the GO structure. The spectral curves facilitate the determination of C/O ratios and the elemental content of both the GO and different GO-MNO$_3$ samples. The C/O ratio is calculated based on the ratio of the peak area of the C element and the peak area of the O element in the test curve. In GO and GO-MNO$_3$, the C element is derived exclusively from the carbon skeleton of the sample. The O atoms derive from oxygen-containing functional groups, nitrate radicals, and adsorbed water molecules. Similarly, C atoms in rGO and rGO-MNO$_3$ come from the carbon skeleton of the sample. In addition, the O element comes from relatively stable oxygen-containing functional groups, nitrite, and small amounts of O from M_2O. Therefore, the change in O element content here includes the results of GO pyrolysis, nitrate salt thermal decomposition, and M_2O formation.

The C/O ratio for the GO sample is 2.07 (Table S2), which is typical of GO [38]. After the introducing process, the C/O ratio of GO-MNO$_3$ exceeded that of the GO sample, indicating that partial reduction of the GO and the OFG of GO were replaced by alkali metal elements [15, 18]. Additionally, a small quantity of nitrate ions is adsorbed onto the surface of the GO and modified GO owing to electrostatic attraction, and hence N peaks are seen in the XPS curves. The nitrates content in the different samples decreases in the order GO-KNO$_3$ > GO-NaNO$_3$ > GO-LiNO$_3$ (Table S2). As is well-known, nitrates undergo thermal decomposition at temperatures above 650 °C, leading to the generation of gases. In this context, the M_2O and CO_2 produced through nitrates decomposition react with C atoms, augmenting the pore structure within the GO nanolayers. This

serves to promote the high-temperature thermal exfoliation of GO. Fig. S6b presents the XPS test results for the samples after thermal exfoliation. The data in Table S2 unambiguously show that subsequent to high-temperature thermal exfoliation, the C content increases across all the samples, and this is accompanied by a substantial decrease in the O content. This indicates that the main mechanism for the elimination of OFG is the thermal exfoliation process, emphasizing the ability of nitrate ions to promote the thermal exfoliation of GO nanosheets.

Fig. 4 illustrates the deconvolution of four bands within the C 1s spectra: the carbon sp^2 and sp^3 (C=C and C–C, 284.6 eV), epoxy (C–O, 286.8 eV), carbonyl (C=O, 287.7 eV), and carboxyl (O=C–OH, 288.9 eV) bands [15]. The COOH content of the samples decreases in the order GO-$LiNO_3$ > GO > GO-KNO_3 > GO-$NaNO_3$ (Table S3). According to our knowledge, cations tend to interact with carboxyl groups of GO and induce the cleavage of the carboxyl and the formation of new C-O and C=C bonds. This process results in increased aromatic C=C group content [32]. In addition, the C=O content in GO decreases after treatment with MNO_3, indicating that M^+ ions also interact with C=O groups to generate complexes, thereby reducing the carbonyl content. Notably, relative to the modified GO samples, GO possesses a low C=C and C–C content, in line with the lower C/O ratio of GO compared to other samples. As illustrated in Fig. 5 and Table S4, the C–C/C=C content of rGO–MNO_3 is greater than that of rGO, indicating that a larger number of OFG in rGO–MNO_3 are involved in the thermal exfoliation process of the sample. These results demonstrate that MNO_3 can facilitate the high-temperature thermal peeling process of GO. Additionally, as observed in Fig. S7, the nitrate band (N element band at a binding energy of 407.6 eV) was transformed into nitrite band (N element band at 403.4 eV) after the high-temperature treatment [39]. This suggests that within the temperature range of 650–800 °C, the nitrate groups were transformed into nitrite groups.

3.5. Adsorption ability of metal ions

As illustrated in Fig. S8, the adsorption performances of GO, rGO, and rGO-KNO_3 for copper metal ions at an initial concentration are presented. The adsorption capacity exhibited a rapid increase over the initial 90 min, which is attributed to the fact that there were a large number of unutilized adsorption sites on the adsorbent, and the adsorbent could rapidly adsorb Cu^{2+} in the aqueous solution. At this stage, the adsorption process is primarily influenced by the kinetic process of diffusion of Cu^{2+} from the liquid phase to the adsorbed phase. The figure illustrates that rGO-

KNO_3 exhibits the highest adsorption rate, followed by rGO and then GO, which exhibits the lowest rate. The reason for this lies in the property of rGO and rGO-KNO_3, which are both mesoporous carbons, allowing rapid diffusion of Cu^{2+} from the liquid phase to the adsorbed phase by the developed mesopores. The mesopores on the surface of GO are relatively low, which inhibits the diffusion rate of Cu^{2+}. After the adsorption time exceeds 90 min, most of the adsorption sites on the adsorbent surface have been occupied by the aqueous solution with Cu^{2+}, resulting in an increase in adsorption resistance and a restriction of the adsorption process. This causes the adsorption capacity curve to begin to increase slowly. The adsorption equilibrium was basically reached after 120 min. Furthermore, the content of OFG on the surface of rGO-KNO_3 and rGO is lower than that of GO, which is not conducive to the adsorption of Cu^{2+}. Consequently, the adsorption capacities of rGO-KNO_3 and rGO (0.89 and 0.78 mmol g^{-1}) are slightly lower than those of GO (1.16 mmol g^{-1}). In addition, the adsorption behavior of the samples was analyzed using two kinetic models (pseudo-first order and pseudo-second order), and the analysis results are shown in Table S5. From Table S5, kinetic studies showed that the adsorption of samples to Cu^{2+} relied on the pseudo-second-order model, and the theoretical value q_e of the equilibrium adsorption amount is also close to the experimental value. Therefore, the adsorption behavior of rGO-KNO_3 belongs to chemical adsorption. From Table S5, it can also be seen that the K_2 of rGO-KNO_3 is larger than that of rGO and GO, which proves that the rGO-KNO_3 has the fastest adsorption rate. Therefore, rGO-KNO_3 with higher mesopore content is suitable for rapid ion adsorption.

3.6. Alkali metal nitrate activation mechanism

To explain the activation effect of the various MNO_3 compounds on GO, we considered different chemical reactions involving MNO_3 and GO that can occur after the incorporation of MNO_3, as illustrated in Fig. 6. Initially, M^+ ions react with hydroxyl, epoxide, and carboxyl groups to form chelates at room temperature. Simultaneously, electrostatic attraction allows nitrate ions to adhere to the GO surface to maintain the charge balance of the system. This process gives rise to two interactions: cation–π interactions and coordination bonds, as illustrated in Fig. 6. GO-MNO_3 can maintain an orderly arranged layered structure with alkali metal nitrate attached to its surface before high-temperature thermal exfoliation. The XRD results in Fig. 2 illustrate this outcome. The heating process can be divided into three distinct stages. In the first stage, with the system temperature

ranging between 100–300 ℃, H_2O molecules adsorbed inside and on the surface of the GO evaporate. Simultaneously, the C atoms of the GO skeleton can react with the oxygen atoms of the surrounding oxygen-containing functional groups to produce CO and CO_2 [40]. As different gases (H_2O, CO, and CO_2) accumulate, a micro-explosion occurs when the internal pressure between the layers of the GO material exceeds the external pressure. The micro-explosion results in thermal exfoliation, transforming much of the condensed GO structure into a new reduced, layered GO structure [12]. At this stage, the thermal exfoliation process is almost complete, which is why many studies recommend heating temperatures of around 350 ℃. During the second heating stage, the temperature increases from 300 to 650 ℃. The stage is primarily concerned with the decomposition of stable OFG. Additional CO and CO_2 will be produced, and the decomposition of OFG will be accompanied by the consumption of some carbon atoms, which will result in the formation of additional pore structures. In the third stage, when the temperature exceeds 650 ℃, the thermal decomposition process of nitrates occurs. Nitrates underwent redox reactions, producing substances such as nitrite, M_2O, and CO_2 [35]. The formation of these substances is accompanied by the creation of more and larger pore structures on the surface of rGO, resulting in the development of micropores into mesopores. Additionally, the arranged GO sheets present a dispersed single-layer structure after high-temperature thermal exfoliation, which can be confirmed by the XRD results of Fig. S3. In conclusion, the aforementioned results elucidate the high-temperature activation process of GO materials initiated by the incorporation of MNO_3 into GO, which ultimately facilitates the formation of mesoporous carbon materials.

4. Conclusions

The introduction of MNO_3 to the surface of GO nanosheets can produce additional CO_2 and CO via thermal decomposition during high-temperature thermal treatment under an Ar flow. The gas production can lead to the creation of additional surface pores on the GO nanosheets, promoting the activation of GO and ultimately generating rGO samples with extremely high mesopore structure content. The SSAs and pore volumes of the different samples decrease in the order rGO-KNO_3 > rGO-$NaNO_3$ > rGO-$LiNO_3$. These findings also underscore the fact that the different MNO_3 have differing effects on GO thermal exfoliation. Consequently, it can be concluded that the incorporation of MNO_3 into GO materials triggers the activation of the high-temperature thermal exfoliation

process, improving the exfoliation efficiency of the GO sample and ultimately increasing the proportion of mesopores. Considering the extraordinarily high mesopore content of rGO-KNO_3, this mesoporous material holds great promise for future applications in water pollution treatment, especially in post-treatment processes aimed at the elimination of heavy metal ions.

CRediT authorship contribution statement

Zhao Li: Conceptualization, Methodology, Validation, Investigation, Data Curation, Visualization, Writing—Original Draft. Moeto Toyoda: Conceptualization, Investigation, Methodology. Takahiro Ohkubo: Conceptualization, Methodology, Resources, Investigation, Methodology, Visualization, Project administration, Supervision, Funding acquisition, Writing—review & editing.

Declaration of Competing Interest

The authors declare that they have no known competing financial interests or personal relationships that could have appeared to influence the work reported in this paper.

Acknowledgments

Funding: This research work was funded by the Japan Society for the Promotion of Science [Grant-in-Aid for Scientific Research C; grant number 15K05645], the Kurita Water and Environment Foundation, and the Salt Science Research Foundation, the Kyoto Technoscience Center.

References

[1] Q. Zhao, B. L. Chen, Concurrent enhancement of structure stability and adsorption capacity of freeze-dried graphene oxide aerogels via the removal of oxidation debris nanoparticles on nanosheets, Environ. Sci. Nano, 8 (2021) 1000–1009.

[2] A. A. Zhou, J. Bai, W. J. Hong, H. Bai, Electrochemically reduced graphene oxide: Preparation, composites, and applications, Carbon, 191 (2022) 301–332.

[3] J. Y. Wu, H. Lin, D. J. Moss, K. P. Loh, B. H. Jia, Graphene oxide for photonics, electronics and optoelectronics, Nat. Rev. Chem., 7 (2023) 162–183.

[4] R. Sakamoto, R. Toyoda, J. Y. Guan, Y. Nishina, K. Kamiya, H. Nishihara, T. Ogoshi, Coordination chemistry for innovative carbon–related materials, Coord. Chem. Rev. 466 (2022) 214577–214600.

[5] K. K. De Silva, H. H. Huang, R. Joshi, M. Yoshimura, Restoration of the graphitic structure by defect

repair during the thermal reduction of graphene oxide, Carbon, 166 (2020) 74–90.
[6] S. Stankovich, D. A. Dikin, R. D. Piner, K. A. Kohlhaas, A. Kleinhammes, Y. Y. Jia, Y. Wu, S. T. Nguyen, R. S. Ruoff, Synthesis of graphene–based nanosheets via chemical reduction of exfoliated graphite oxide, Carbon, 45 (2007) 1558–1565.
[7] C. Zhang, W. Lv, X. Y. Xie, D. M. Tang, C. Liu, Q. H. Yang, Towards low temperature thermal exfoliation of graphite oxide for graphene production, Carbon, 62 (2013) 11–24.
[8] Y. Qiu, S. Moore, R. Hurt, I. Külaots, Influence of External Heating Rate on the Structure and Porosity of Thermally Exfoliated Graphite Oxide, Carbon, 111 (2017) 651–657.
[9] Y. Qiu, F. Collin, R. H. Hurt, I. Külaots, Thermochemistry and kinetics of graphite oxide exothermic decomposition for safety in large–scale storage and processing, Carbon, 96 (2016) 20–28.
[10] L. Song, F. Khoerunnisa, W. Gao, W. H. Dou, T. Hayashi, K. Kaneko, M. Endo, P. M. Ajayan, Effect of high–temperature thermal treatment on the structure and adsorption properties of reduced graphene oxide, Carbon, 52 (2013) 608–612.
[11] I. Sengupta, S. Chakraborty, M. Talukdar, S. K. Pal, S. Chakraborty, Thermal reduction of graphene oxide: How temperature influences purity, J. Mater. Sci., 33 (2018) 4113–4122.
[12] Y. Qiu, F. Guo, R. Hurt, I. Külaots, Explosive thermal reduction of graphene oxide–based materials: mechanism and safety implications, Carbon, 72 (2014) 215–223.
[13] O. Jankovský, P. Marvan, M. Nováček, J. Luxa, V. Mazánek, K. Klímová, D. Sedmidubský, Z. Sofer, Synthesis procedure and type of graphite oxide strongly influence resulting graphene properties, Appl. Mater. Today, 4 (2016) 45–53.
[14] H. Ramamoorthy, K. Buapan, T. Chiawchan, K. Thamkrongart, R. Somphonsane, Exploration of the temperature–dependent correlations present in the structural, morphological and electrical properties of thermally reduced free–standing graphene oxide papers, J. Mater. Sci., 56 (2021) 15134–15150.
[15] S. Naghdi, H. Y. Song, A. Várez, K. Y. Rhee, S. W. Kim, Engineering the electrical and optical properties of graphene oxide via simultaneous alkali metal doping and thermal annealing, J. Mater. Res. Technol., 9 (2020) 15824–15837.
[16] E. T. Mombeshora, P. G. Ndungu, V.O. Nyamori, Effect of graphite/sodium nitrate ratio and reaction time on the physicochemical properties of graphene oxide, New Carbon Materials, 32 (2017) 174–187.
[17] S. J. Yang, T. Kim, H. Jung, C. R. Park, The effect of heating rate on porosity production during the low temperature reduction of graphite oxide, Carbon, 53 (2013) 73–80.
[18] L. Chen, G. P. Shi, J. Shen, B. Q. Peng, B. W. Zhang, Y. Z. Wang, F. G. Bian, J. J. Wang, D. Y. Li, Z. Qian, G. P. Xu, G. Liu, J. R. Zeng, L. J. Zhang, Y. Z. Yang, G. Q. Zhou, M. H. Wu, W. Q. Jin, J. Y. Li, H. P. Fang, Ion sieving in graphene oxide membranes via cationic control of interlayer spacing, Nature, 550 (2017) 380–383.
[19] S. Mecozzi, A. P. West, D. A. Dougherty, Cation–π Interactions in Simple Aromatics: Electrostatics Provide a Predictive Tool, J. Am. Chem. Soc., 118 (1996) 2307–2308.
[20] W. S. Hummers, R. E. Offeman, Preparation of Graphitic Oxide, J. Am. Chem. Soc., 80 (1958) 1339–1339.
[21] Y. Xu, L. Zhao, H. Bai, W. Hong, C. Li, G. Shi, Chemically Converted Graphene Induced Molecular Flattening of 5,10,15,20-Tetrakis (1-methyl-4-pyridinio) porphyrin and Its Application for Optical Detection of Cadmium(II) Ions, J. Am. Chem. Soc., 131 (2009) 13490–13497.
[22] N. Setoyama, T. Suzuki, K. Kaneko, Simulation study on the relationship between a high resolution α_s–plot and the pore size distribution for activated carbon, Carbon, 36 (1998) 1459–1467.
[23] K. Kaneko, C. Ishii, Superhigh surface area determination of microporous solids, Colloids and

Surfaces, 67 (1992) 203–212.
[24] M. Thommes, K. Kaneko, A. V. Neimark, J. P. Olivier, F. Rodriguez–Reinoso, J. Rouquerol, K. S. W. Sing, Physisorption of gases, with special reference to the evaluation of surface area and pore size distribution (IUPAC Technical Report), Pure Appl. Chem., 87 (2015) 1051–1069.
[25] M. S. Yilmaz, Graphene oxide/hollow mesoporous silica composite for selective adsorption of methylene blue, Microporous Mesoporous Mater., 330 (2022) 111570–111580.
[26] J. Lee, H. Kim, A. Kim, H. Jung, Nitrogen–doped mesoporous graphene with fine–tuned pore size in a few nanometer–scale for supercapacitor applications, Microporous Mesoporous Mater., 293 (2020) 109794–109802.
[27] B. Tansel, Significance of thermodynamic and physical characteristics on permeation of ions during membrane separation: Hydrated radius, hydration free energy and viscous effects, Sep. Purif. Technol., 86 (2012) 119–126.
[28] H. Zhou, D. Zhang, Effects of interactions with metal ions on the thermal reduction of graphene oxide, J. Phys. Chem. Solids., 154 (2021) 110090–110100.
[29] Y. Z. Shi, X. Y. Ren, H. Zheng, Y. Zhang, Q. Zuo, Hierarchical 13X zeolite/reduced graphene oxide porous material for trace Pb (II) capturing from drinking water, Microporous Mesoporous Mater., 329 (2022) 111540–111550.
[30] R.N. Kust, J.D. Burke, Thermal decomposition in alkali metal nitrate melts, Inorganic and Nuclear Chemistry Letters, 6 (1970) 333–335.
[31] O. Abe, T. Utsunomiya, Y. Hoshino, The thermal stability of binary alkali metal nitrates, Thermochimica Acta, 78 (1984) 251–260.
[32] S. Park, K. S. Lee, G. Bozoklu, W. Cai, S. T. Nguyen, R. S. Ruoff, Graphene Oxide Papers Modified by Divalent Ions–Enhancing Mechanical Properties via Chemical Cross–Linking, ACS Nano, 2 (2008) 572–578.
[33] R. Castaldo, G. C. Lama, P. Aprea, G. Gentile, M. Lavorgna, V. Ambrogi, P. Cerruti, Effect of the oxidation degree on self–assembly, adsorption and barrier properties of nano–graphene, Microporous Mesoporous Mater., 260 (2018) 102–115.
[34] T. Ohkubo, H. Nakayasu, Y. Takeuchi, N. Takeyasu, Y. Kuroda, Acidic layer–enhanced nanoconfinement of anions in cylindrical pore of single–walled carbon nanotube, J. Colloid Interface Sci., 629 (2022) 238–244.
[35] H. Wang, R. Shen, Y. Ye, L. Wu, Thermal behaviour and decomposition reaction kinetics of graphite/potassium nitrate, Chin. J. Energ. Mater., 20 (2012) 731–734.
[36] J. Ma, C. Liu, F. Pu, M. Wang, S. Tian, H. Li, H. Zheng, L. Wang, C. Wang, C. Yang, H. Liu, L. An, C. Song, Y. Wang, Constructing pore arrays on nitrogen–doped carbon to boost potassium–ion storage capacity, Microporous Mesoporous Mater., 341 (2022) 112076–112086.
[37] J. H. Wee, Y. A. Kim, C. M. Yang, Sequential doping of nitrogen and oxygen in single–walled carbon nanohorns for use as supercapacitor electrodes, Microporous Mesoporous Mater., 310 (2021) 110595–110601.
[38] J. Park, W. Lee, J. Nam, J. T. Han, C. J. Choi, J. Y. Hwang, A study of the correlation between the oxidation degree and thickness of graphene oxides, Carbon, 189 (2022) 579–585.
[39] Y. C. Lin, Y. Y. Chen, B. Y. Yu, W. C. Lin, C. H. Kuo, J. J. Shyue, Sputter-induced chemical transformation in oxoanions by combination of C_{60}^{+} and Ar^{+} ion beams analyzed with X-ray photoelectron spectrometry, The Analyst, 134 (2009) 945–951.
[40] J. C. Wang, S. Kaskel, KOH activation of carbon–based materials for energy storage, J. Mater.

Chem., 22 (2012) 23710–23725.

Tables

Table 1. Specific surface areas and pore volumes of rGO-$LiNO_3$, rGO-$NaNO_3$, rGO-KNO_3, and rGO.

Samples	a_{total}[a] / $m^2\ g^{-1}$	$W_{micro+meso}$[b] / $cm^3\ g^{-1}$	Micropore		Mesopore		a_{meso}/a_{micro}	W_{meso}/W_{micro}
			a_{micro}[c] / $m^2\ g^{-1}$	W_{micro}[d] / $cm^3\ g^{-1}$	a_{meso}[e] / m^2	W_{meso}[f] / $cm^3\ g^{-1}$		
rGO-$LiNO_3$	325	0.99	20	0.048	305	0.95	15.2	19.8
rGO-$NaNO_3$	341	1.09	21	0.051	320	1.04	15.2	20.4
rGO-KNO_3	359	1.26	23	0.054	336	1.21	14.6	22.4
rGO	206	0.61	18	0.043	188	0.57	10.4	13.2

[a]Total specific surface area. [b]Total pore volume of micropore and mesopore obtained from each isotherm at $P/P_0 = 0.95$. [c]Micropore specific surface area. [d]Micropore volume. [e]Mesopore specific surface area. [f]Mesopore volume.

Table 2. Structural parameters obtained from XRD data.

Samples	2θ / deg.	FWHM / deg.	d spacing / nm
GO-$LiNO_3$	11.70	0.939	0.756
GO-$NaNO_3$	11.92	0.765	0.742
GO-KNO_3	11.55	0.802	0.766
GO	11.45	0.732	0.773

Table 3. Detailed composition data obtained from TG analysis of GO-$LiNO_3$, GO-$NaNO_3$, GO-KNO_3, and GO.

Samples	Adsorbed water / wt %	Unstable OFG / wt %	Stable OFG / wt %	Degradation of MNO_3 / wt %	Residual weight / wt %
GO-$LiNO_3$	14.55	27.28	18.36	11.43	28.38
GO-$NaNO_3$	12.6	25.44	16.58	11.33	34.05
GO-KNO_3	11.21	26.73	17.71	12.97	31.38
GO	13.28	35.21	14.94	N/A	36.57

Figure captions

Fig. 1. N_2 adsorption–desorption isotherms of rGO-$LiNO_3$, rGO-$NaNO_3$, rGO-KNO_3, and rGO.

Fig. 2. (a) XRD patterns and (b) FTIR spectra of GO-$LiNO_3$, GO-$NaNO_3$, GO-KNO_3, and GO.

Fig. 3. TG curves of GO-$LiNO_3$, GO-$NaNO_3$, GO-KNO_3, and GO.

Fig. 4. High-resolution C 1s XPS spectra of GO-$LiNO_3$ (a), GO-$NaNO_3$ (b), GO-KNO_3 (c), and GO (d).

Fig. 5. High-resolution C 1s XPS spectra of rGO-$LiNO_3$ (a), rGO-$NaNO_3$ (b), rGO-KNO_3 (c), and rGO (d).

Fig. 6. Schematic diagram of the *M*NO_3-activated GO thermal exfoliation mechanism.

Figures

Fig. 1

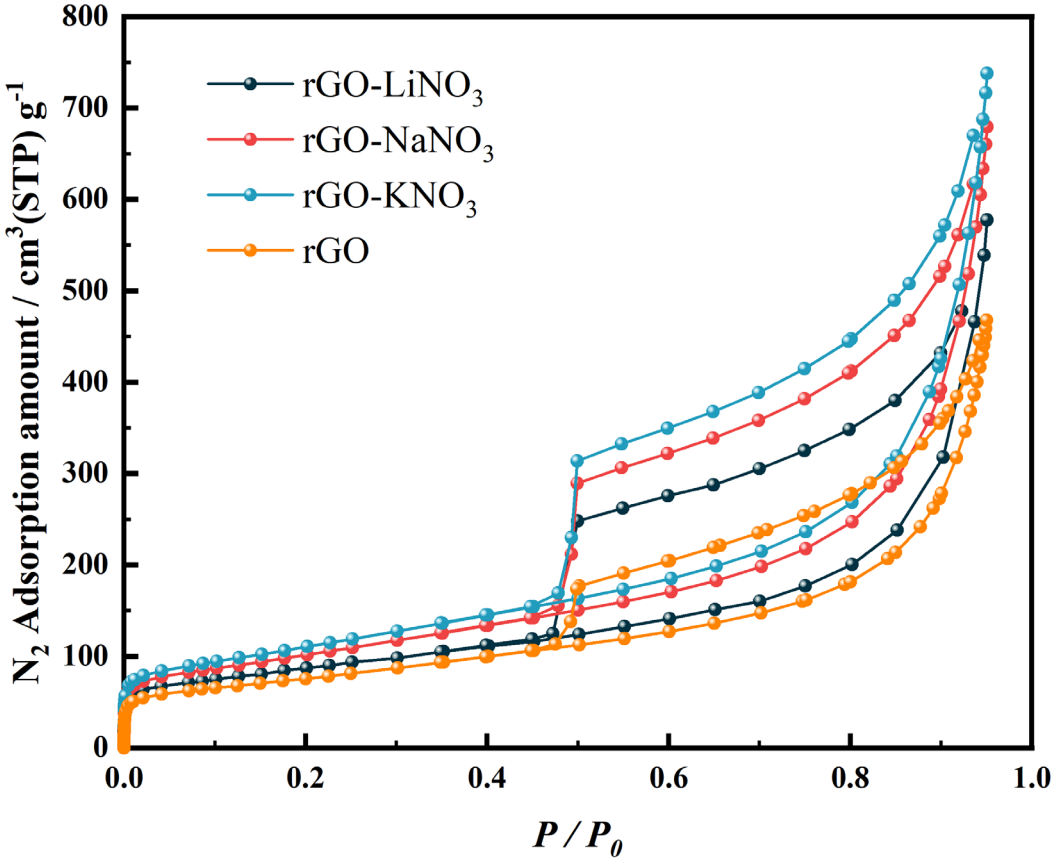

Fig. 2

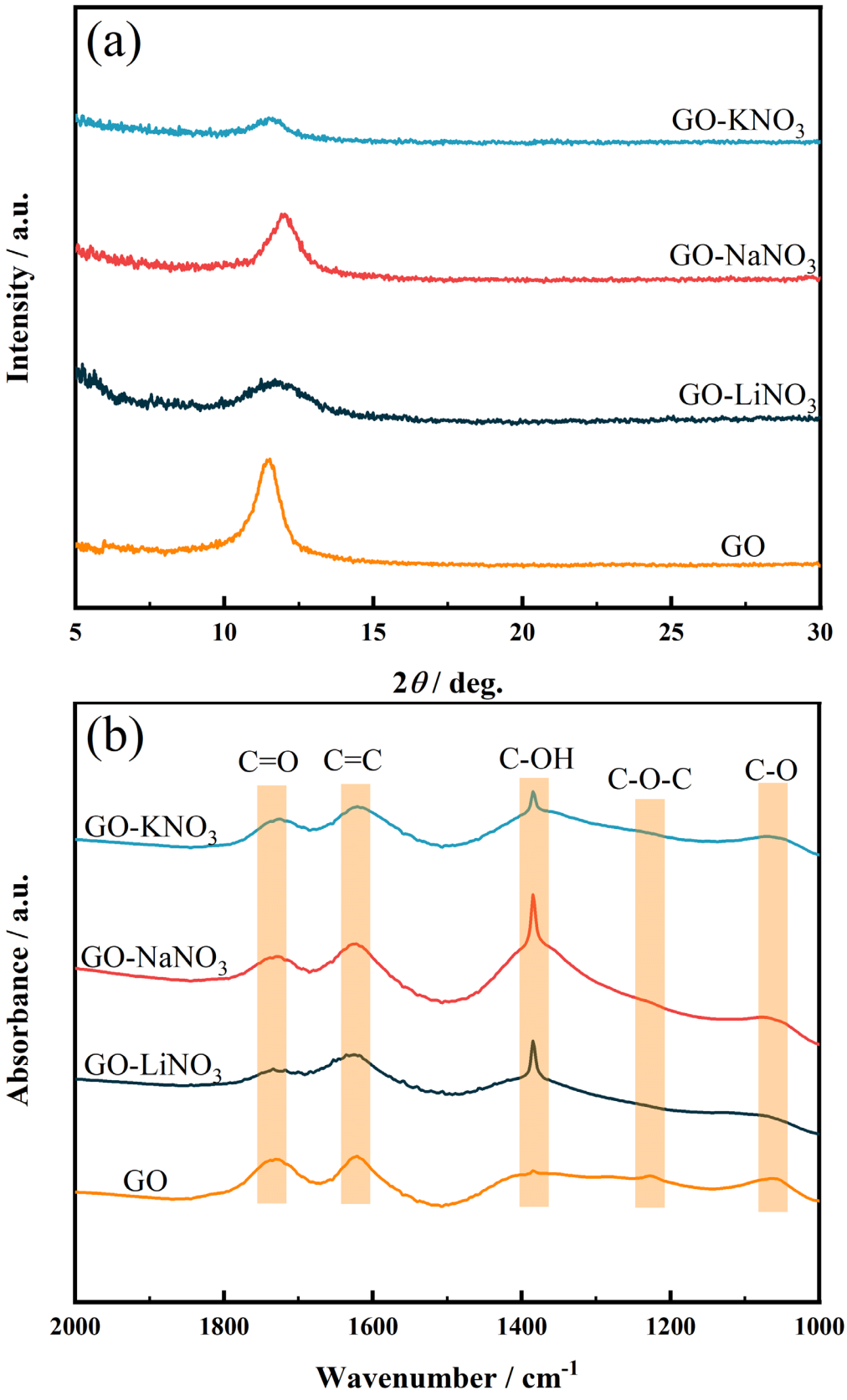
(a)
GO-KNO3
GO-NaNO3
GO-LiNO3
GO
Intensity / a.u.
5
10
15
20
25
30
2θ / deg.
(b)
C=O
C=C
C-OH
C-O-C
C-O
GO-KNO3
GO-NaNO3
GO-LiNO3
GO
Absorbance / a.u.
2000
1800
1600
1400
1200
1000
Wavenumber / cm-1

Fig. 3

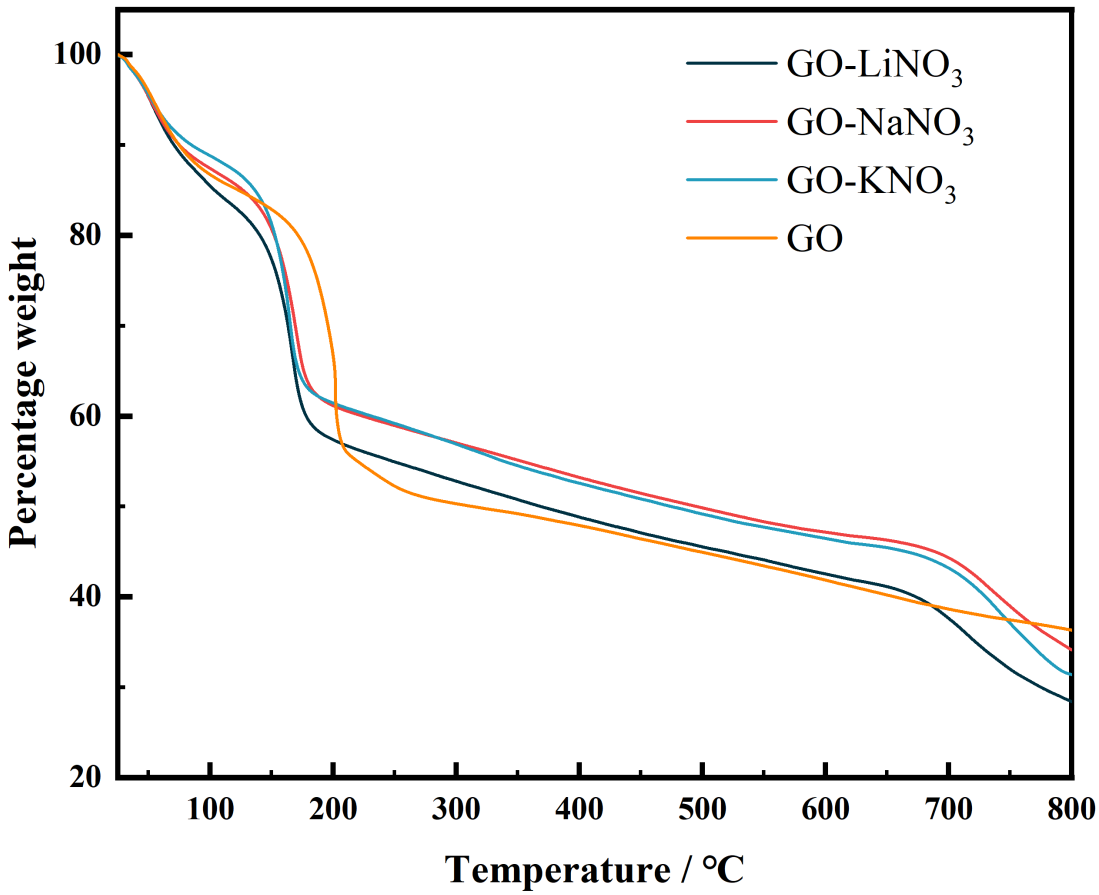
GO-LiNO3
GO-NaNO3
GO-KNO3
GO
Percentage weight
100
80
60
40
20
100
200
300
400
500
600
700
800
Temperature / ℃

Fig. 4

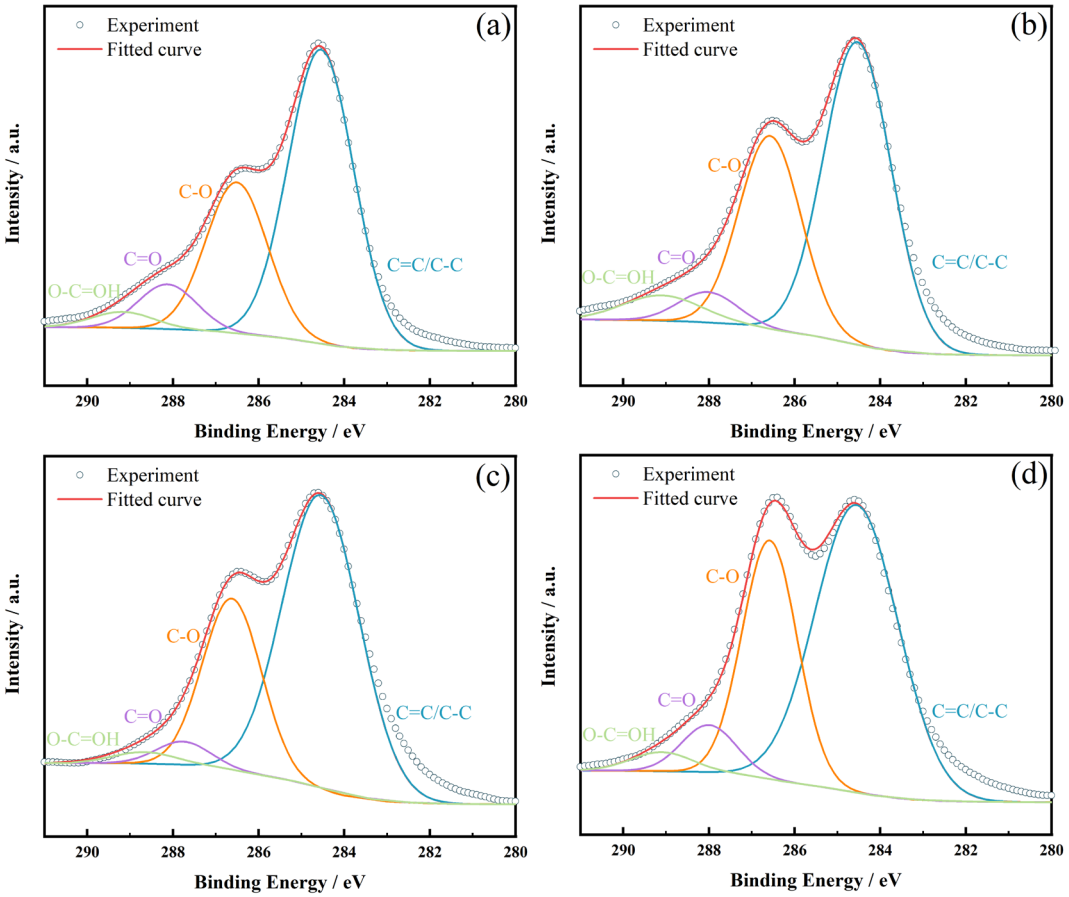
(a)
(b)
(c)
(d)
Experiment
Fitted curve
C-O
C=O
O-C=OH
C=C/C-C
Intensity / a.u.
Binding Energy / eV
290
288
286
284
282
280

Fig. 5

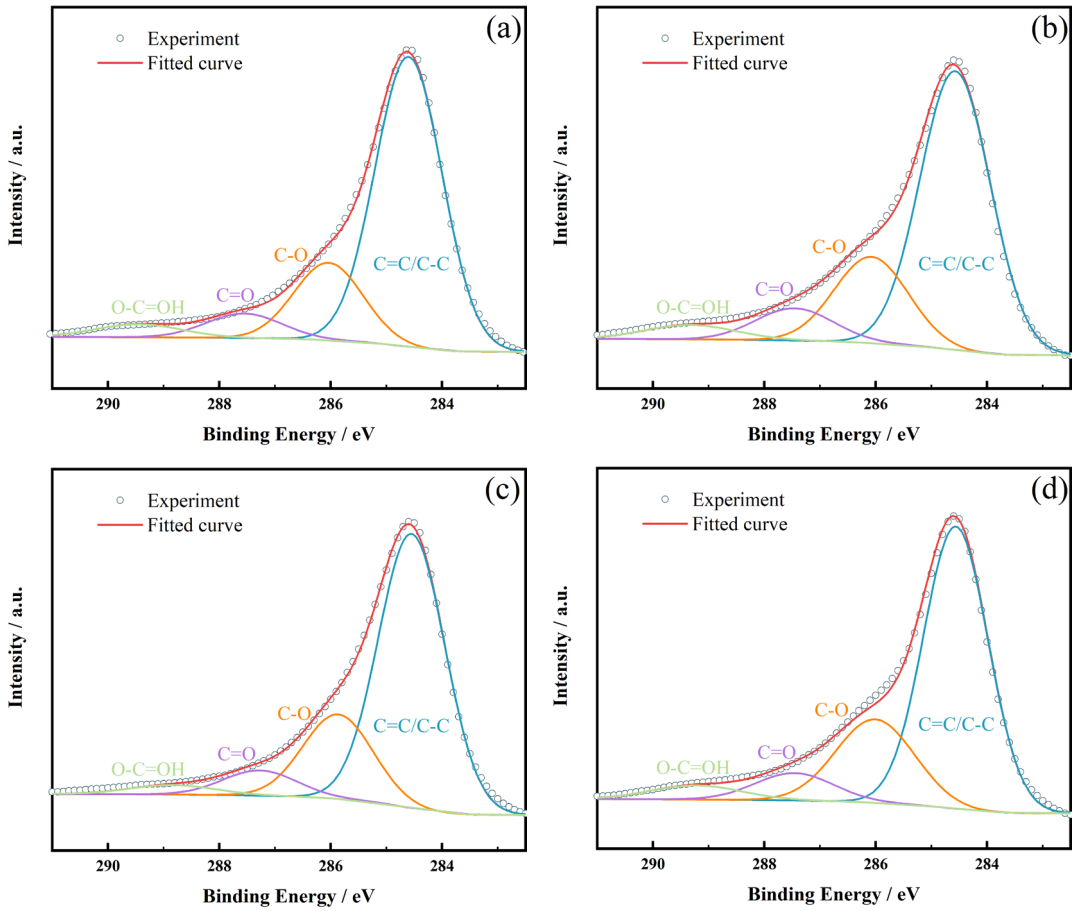
(a)
(b)
(c)
(d)
Experiment
Fitted curve
O-C=OH
C=O
C-O
C=C/C-C
Intensity / a.u.
Binding Energy / eV
290
288
286
284

Fig. 6

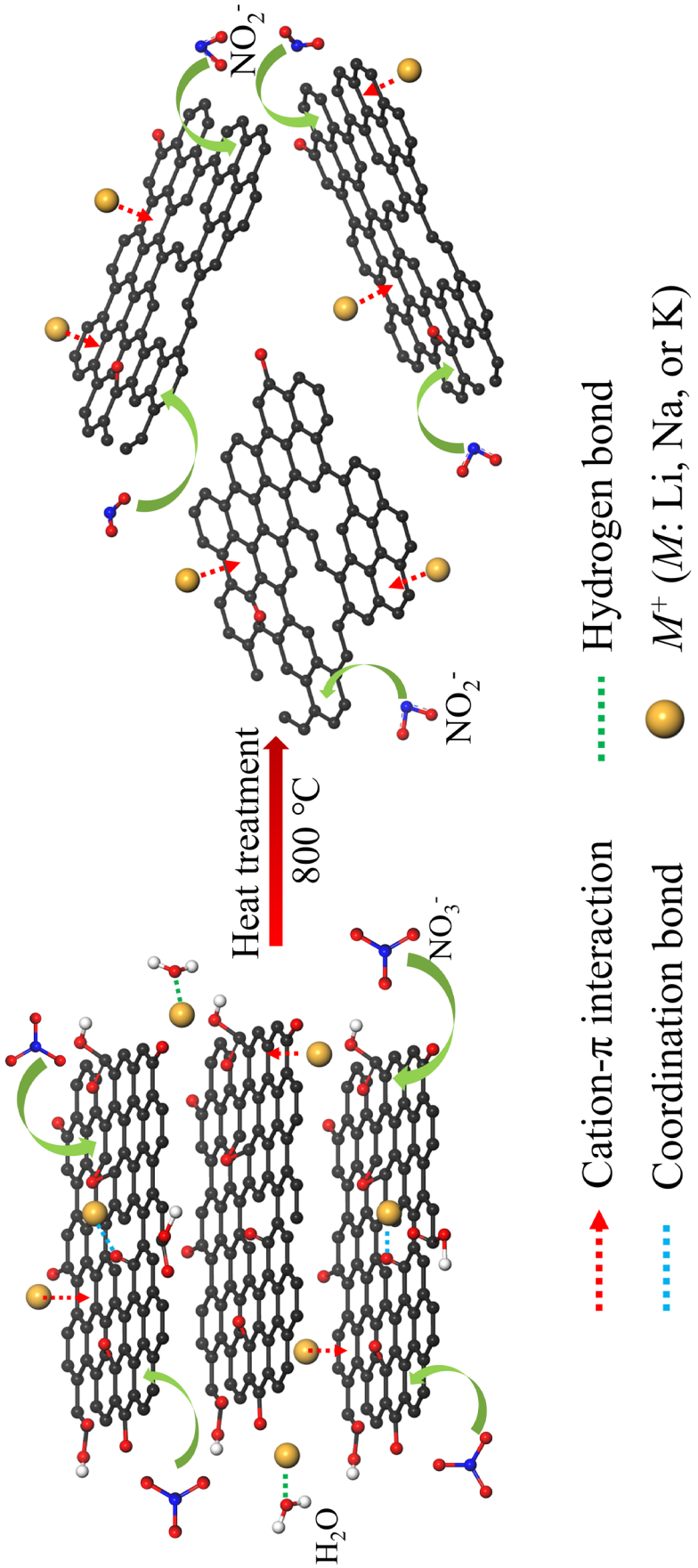
NO_2^-
NO_2^-
Heat treatment
800 °C
NO_3^-
H_2O
Cation-π interaction
Hydrogen bond
Coordination bond
M^+ (*M*: Li, Na, or K)